



Pyrolysis characteristics, kinetics, and biochar of fermented pine sawdust-based waste

Yiteng Zhang^{1,2} · Jun Hu^{1,2} · Xingxing Cheng^{1,2} · Mudassir Hussain Tahir³

Received: 17 September 2022 / Accepted: 27 December 2022 / Published online: 5 January 2023
© The Author(s), under exclusive licence to Springer-Verlag GmbH Germany, part of Springer Nature 2023

Abstract

The objective of current study is to explore the energy recovery potential of fermentation residues. In this perspective, pyrolysis characteristics, kinetics, and modified biochar derived from pine sawdust after fermentation (FPD) were determined, and comparison was established with pine sawdust (PD). The variation range of comprehensive pyrolysis index (CPI) values of FPD was found 6.51×10^{-7} – $16.38 \times 10^{-7} \%^2 \cdot \text{min}^{-2} \cdot \text{C}^{-3}$, significantly higher than that of untreated samples determined under the same experimental conditions. The average activation energy of FPD was 367.95 kJ/mol, 389.45 kJ/mol, and 346.55 kJ/mol calculated by Flynn–Wall–Ozawa (FWO) method, Kissinger-Akahira-Sonuse (KAS), and Starink method respectively, and importantly, these values are much higher than those of PD. Additionally, fermentation could enhance the adsorption capacity for methylene blue of biochar from 0.76 mg/g to 1.6 mg/g due to the abundant surface functional groups and three-dimensional internal pore structure. The adsorption pattern of fermented pine wood shifted from chemisorption dominated to the synergetic adsorption of surface functional groups adsorption and intragranular filling. These results show that FPD has favorable pyrolytic properties, and the derived biochar has adsorption properties, which is the basis for designing pyrolysis process and reusing fermentation residues.

Highlights The FPD has higher values of CPI and activation energy than the PD.

FPD-derived biochar has higher adsorption capacity than PD-derived biochar.

The fermentation improves the pyrolysis performance.

The fermentation enhances adsorption capacity due to unique structure of biochar.

Keywords Fermentation · Pine sawdust · Pyrolysis · Biochar · Adsorption

Introduction

Rapid development of daily life leads to high energy consumption and the depletion of traditional fossil fuels. Searching for new renewable energy sources and making efficient use of traditional energy are the two main directions of energy systems (Liu et al. 2022; Zhang et al. 2022b).

Recently, biomass as a kind of low-cost and abundant resource has attracted much researcher's attention all over the world because of alleviating energy pressure and greenhouse gas emissions associated with environmental issue (Ahmad et al. 2019; Yu et al. 2022).

Currently, the major biomass conversion technologies are incineration, pyrolysis (Feng et al. 2022), hydrothermal (Wang et al. 2021), fermentation composting, and fine chemical production (Nenciu et al. 2021). The incineration method requires high operation cost and energy consumption on flue gas treatment. Meanwhile, the landfill method could result in land occupation and risk of secondary pollution. Moreover, engineering and economic feasibility of fine chemicals productions have yet not been fully demonstrated. Remarkably, fermentation is an important method of biomass waste reutilization to produce biofuel, fertilizers, and combustible gas energy with a large amount of fermentation wastes

Responsible Editor: Zhihong Xu

✉ Xingxing Cheng
xcheng@sdu.edu.cn

¹ School of Energy and Power Engineering, Shandong University, Jinan 250061, China

² National Engineering Laboratory for Reducing Emissions From Coal Combustion, Jinan 250061, China

³ Graduate School of Energy Science, Kyoto University, Yoshida-Honmachi, Sakyo-Ku, Kyoto 606-8501, Japan

(Barzallo-Bravo et al. 2019; Wang et al. 2022). Importantly, fermentation technology deals with both techniques, i.e., aerobic and anaerobic methods (Ma and Liu 2019). Fermentation residues contain some useful components such as proteins, carbohydrates, and trace compounds, which are widely used in substrate culture (Gupta et al. 2022). Fermented sawdust substrate may be a suitable potting medium for plant growth (Hoang et al. 2019), seed germination (Ahn et al. 2021), mushroom cultivation (He et al. 2022), etc. Ultimately, if they were not handled skillfully, it might cause serious environmental pollution and importantly, energy waste. Thus, the approaches for reusing or handling fermentation waste are urgently required (Wang et al. 2021).

Pyrolysis technologies are mainly used for value-added products that involve the conversion of organic materials into solids (biochar), condensable liquids (bio-oil), and non-condensable volatiles (gases) (Amenaghawon et al. 2021, Buessing and Goldfarb 2012). Biochar has been widely used in environmental remediation, such as soil improvement, waste water treatment, and antibiotic removal. The absorption capacity of the biochar derived from timber industry wood is found 229 mg/g and 210 mg/g at 45°C and 25°C, respectively (Herath et al. 2022). Yang et al. (Li et al. 2022) found that activated biochar derived from corncob xylose residue possessed a high surface area of 3043 m²/g and an adsorption capacity of 1429 mg/g which are highly useful to remove antibiotics from waste water. Furthermore, stillage residue-derived biochar was observed to remove silver ions from aqueous solutions with a maximum capacity of 90.06 mg/g (Yao et al. 2015). Moreover, biochars resulted from fermentation residues had been used to make soil remediation agents (Wang et al. 2022) and heavy metal adsorbents (Zhang et al. 2017). It reflects that applying pyrolysis to produce biochar from fermentation residues could be an effective approach to reduce environment issues and recycling biomass energy.

Previously, pyrolysis of pine sawdust to investigate basic characteristics had been performed (Gao et al. 2013; Tian et al. 2021; Zhang et al. 2022a). However, only a few studies can be found associated with pyrolysis process and potential application of biochar derived from fermentation pine sawdust. So, in this study, fermented pine sawdust (FPD) was used as a representative of fermentation residue. The primary purposes of this research were to investigate (1) bioenergy recovery potential of fermented biomass waste during pyrolysis process and (2) industry and elemental analysis. In current research study, pine sawdust (PD) was used as reference material, and the matrix of FPD was based on PD. Besides, the biochars were characterized to explore the effects of fermentation on pore structure

formation and surface functional group distribution. Moreover, the applicability of biochar by methylene blue (MB) adsorption experiments was also tested. Overall, the results of this investigation can provide a better understanding of fermented pine sawdust pyrolysis behaviors and basis for recovery of the biomass energy of fermentation residues.

Material and methods

Materials and characterization

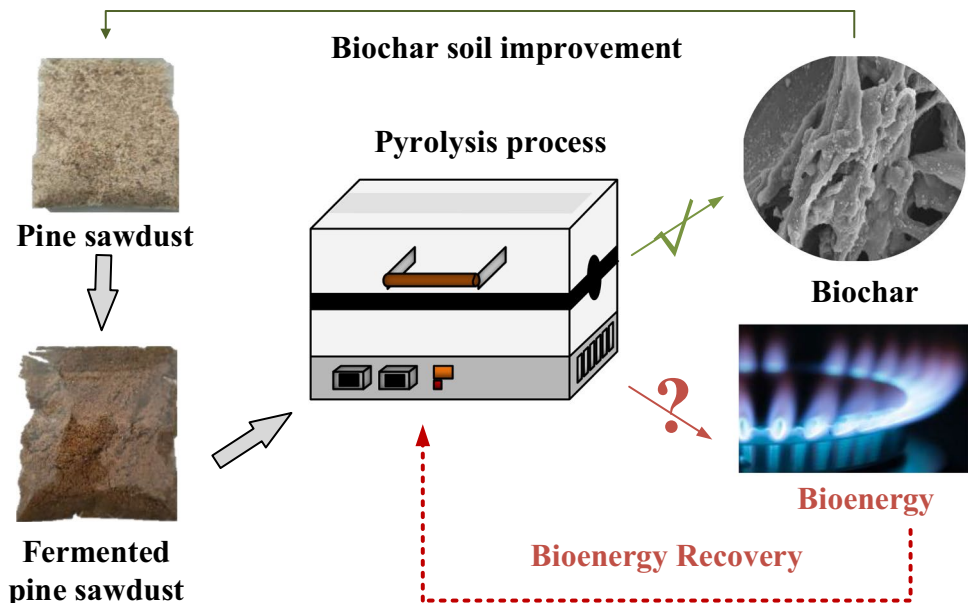
PD were taken from a wood processing plant in Xingtai (Hebei, China), and FPD were derived from the mixed fermentation of yeast and pine sawdust at a mass ratio of 1:20 for 15 days at 30°C. The total nitrogen content, amino nitrogen content, and solid content of yeast extract were 6.5%, 2.0%, and 60%, respectively. The PD and FPD were dehydrated at 105°C using an oven and grinded into fine powders (20–40 mesh). An industrial analyzer (SDTGA5000) was used for proximate analysis to determine the volatiles (V), moisture (M), fixed carbon (FC), and ash (A) contents. The composition of C/H/N/S/O in the PD and FPD samples was determined with elemental analyzer (Vario MACROCHN).

Pyrolysis characteristics and experimental process

As shown in Fig. 1, pyrolysis characteristics of PD and FPD were analyzed in terms of mass loss using a TG analyzer (TGA/DSC, METTLER Company) with flow of high purity N₂ (≥99.99%). Samples about 10 mg were distributed in open alumina crucible and heated from 30 to 800 °C with ramp rates of 20 °C/min, 30 °C/min, 40 °C/min, and 50 °C/min, under a flow rate of 50 mL/min. The thermogravimetric data for kinetic calculation were collected and processed following ICTAC Kinetics Committee recommendations. Meanwhile, the corresponding samples were designated as PD-X or FPD-X, where X represents the different pyrolysis heating rates. In addition, the PD and FPD were put into a fast-annealing furnace to pyrolyze at 500 °C, 600 °C, 700 °C, and 800 °C at a flow rate of 300 mL/min for 60 min. The samples of pyrolytic char were collected and named as PD-X or FPD-X (X represents final temperatures). In addition, the comprehensive pyrolysis index (CPI) is introduced to evaluate the pyrolysis behavior (Eq. (1)) (Bi et al. 2021), the meaning of each letter in the formula has been clarified in Table 2.

$$CPI = \frac{DTG_{\max} DTG_{\text{mean}} M_{\infty}}{T_i T_p \Delta T_{1/2}} \quad (1)$$

Fig. 1 The pyrolysis process of PD and FPD



Pyrolysis kinetic models

In this section, the fundamental rate equation (Eq. (2) and Eq. (3)) (Borel et al. 2020; Chhabra et al. 2019) is used in the pyrolysis kinetics calculations.

$$\frac{d\alpha}{dt} = k(T)f(\alpha) = A \exp\left(-\frac{E_\alpha}{RT}\right) f(\alpha) \tag{2}$$

$$\alpha = \frac{m_0 - m_t}{m_0 - m_r} \tag{3}$$

where $k(T)$ is the rate constant and $f(\alpha)$ is the reaction model function, which is $f(\alpha) = (1-\alpha)^n$. E_α is the activation energy. R expresses the general gas constant ($R = 8.314 \text{ J}\cdot\text{mol}^{-1}\cdot\text{K}^{-1}$). T stands for the reaction temperature. t represents the reaction time, and α is the conversion ratio. m_0 , m_p , and m_r are the initial, instantaneous, and residue weights of the sample, respectively.

Equation (2) was simplified to obtain Eq. (4), and the calculation formula (Eq. (5)) for $g(\alpha)$ was obtained (Khiri et al. 2019, Sarkar and Wang 2020, Soria-Verdugo et al. 2020).

$$\frac{d\alpha}{dT} = \frac{A}{\beta} \exp\left(-\frac{E_\alpha}{RT}\right) f(\alpha) \tag{4}$$

$$g(\alpha) = \int_0^\alpha \frac{d\alpha}{f(\alpha)} = \frac{A}{\beta} \int_{T_0}^T \exp\left(-\frac{E_\alpha}{RT}\right) dT \tag{5}$$

Three thermolysis kinetic models were used in this paper to evaluate the activation energies of the reactions—Eqs. (6, 7, 8) (Meng et al. 2015; Ni et al. 2022; Zhang et al. 2019).

$$\text{KASmodel} : \ln\left(\frac{\beta}{T^2}\right) = \ln\left(\frac{AR}{E_\alpha g(\alpha)}\right) - \frac{E_\alpha}{RT} \tag{6}$$

$$\text{FWOmodel} : \ln\beta = \left(\frac{AE_\alpha}{Rg(\alpha)}\right) - 5.331 - 1.052 \frac{E_\alpha}{RT} \tag{7}$$

$$\text{Starinkmodel} : \ln\left(\frac{\beta}{T^{1.92}}\right) = C - 1.0008 \frac{E_\alpha}{RT} \tag{8}$$

Thereafter, thermodynamic assessment thermodynamic parameters (Agnihotri et al. 2022; Fu et al. 2022) were for thermodynamic evaluation.

$$A = \frac{E \times \beta \times \exp\left(\frac{E}{T_p \times R}\right)}{T_p^2 \times R} \tag{9}$$

$$\Delta H = E - R \times T_\alpha \tag{10}$$

$$\Delta G = R \times T_p \times \ln\left(\frac{K_B \times T_p}{A_0 \times h}\right) + E \tag{11}$$

$$\Delta S = \frac{(\Delta H - \Delta G)}{T_p} \tag{12}$$

where T_p denotes the average peak absolute temperature obtained from DTG plot and K_B and h are the Boltzmann constant (1.381×10^{-23} J/K) and the Planck's constant (6.626×10^{-34} J·s), respectively.

Characteristic analysis of biochar

The surface morphology of biochar was examined using a scanning electron microscopy (SEM) (JEOL JSM-6700F, Japan). The Fourier transform infrared spectra ($4000\text{--}400\text{ cm}^{-1}$) were collected at a resolution of 4 cm^{-1} with 16 scans co-added using a Nicolet 6700 FTIR (Thermo Electron Corporation, USA). Besides, biochar samples were tested for adsorption applications. A 0.1-g adsorbent was added to 100-mL MB solution (5 mg/L) stirring with a magnetic stirrer to promote the reaction (25 °C) and sampled for the determination of MB concentration using an ultraviolet spectrophotometer (V-1200 MAPADA, Shanghai) at 665 nm. The standard curve of MB determined was demonstrated in Eq. (13), and the amount of MB adsorbed at equilibrium (q_e (mg/g)) was calculated by the Eq. (14) (Liu et al. 2021). Other adsorption model calculation formulas are shown in Table 5.

$$Y = 6.54X - 0.604 (R^2 = 0.999) \quad (13)$$

$$q_e = \frac{C_0 - C_e}{W} V \quad (14)$$

where X is the absorbance of MB, Y is the concentration of MB solution (mg/L), q_e (mg/g) is the adsorption capacity, C_0 (mg/L) and C_e (mg/L) are the initial and equilibrium concentration, respectively, V is the volume of MB solution and W is the mass of PD-X or FPD-X.

Results and discussions

Characterization of PD and FPD

The proximate and ultimate analyses of PD and FPD are shown in Table 1. The ash content of FPD is 4.48%, higher than that of PD (1.86%) in the present study, but lower than that of the reported biomasses (Tao et al. 2021; Zhang et al. 2022b) such as rice straw (16.90%), cabbage waste (12.98%), and cotton stalk (15.60%). The volatile content is 73.89%, lower than that of PD (81.77%) while fixed carbon is 21.63%, respectively. The results clearly demonstrate that fermentation would affect the products' properties due to the change of volatile content, ash content, and fixed carbon content. For example, the ash composition of biomass was made up of inorganic salts and oxides, and the inorganic salts and oxides, and these constituents may catalyze

Table 1 Physicochemical characterization of PD and FPD

Project	PD (wt%)	FPD (wt%)
(Volatiles) _d ^a	81.77	73.89
(Fixed carbon) _d	16.35	21.63
(Ash) _d	1.86	4.48
(LHV) _d (MJ/kg)	19.59	19.22
(Carbon) _d	44.75	31.59
(Hydrogen) _d	5.77	5.12
(Oxygen) _d ^b	49.21	62.20
(Nitrogen) _d	0.15	0.93
(Sulfur) _d	0.12	0.16

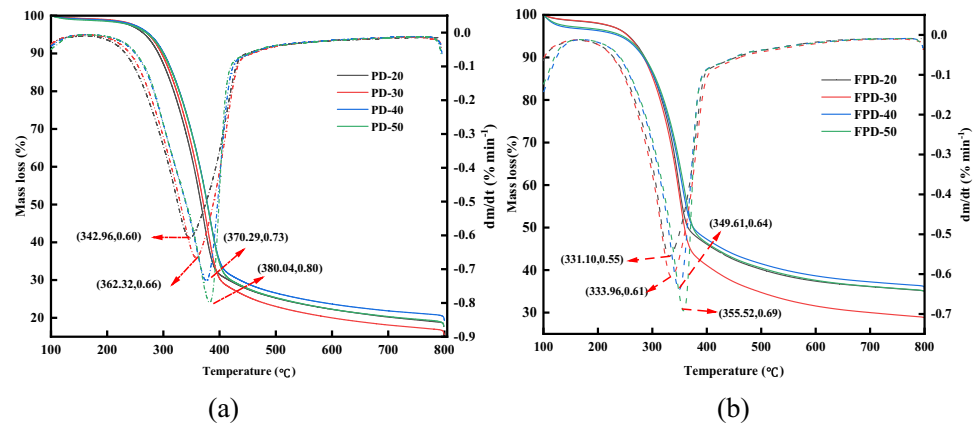
LHV, low heating value; ^ad indicates the abbreviation of "dry basis"; ^bcalculated by difference.

and promote pyrolysis process, thus affecting the yield of pyrolytic products. The elemental analysis showed that C and O were the major elements contained in FPD, which accounted for 31.59 and 62.20%, respectively, the contents of H and N were 5.12 and 0.93%, and the content of S was only 0.16%. The contents of O and N in FPD were higher, but C was lower than those in PD, which might be attributed to residue sediments including proteins and amino acids and fermentation by-products on the PD during the process of microbial fermentation. The high heating value is 19.22 MJ kg^{-1} , which is higher than that of some terrestrial biomass feedstock, such as cabbage waste (17.29 MJ kg^{-1}), rice husk (16.24 MJ kg^{-1}), and pea waste (18.42 MJ kg^{-1}). These results confirm that FPD is favorable when considered for a pyrolysis process.

Pyrolysis characteristics of PD and FPD

The TG/DTG curves of samples at different heating rates are shown in Fig. 2. Although the compositions of PD and FPD were different, they had similar mass loss trend. The main pyrolysis process could be divided into four stages: water devolatilization, active pyrolysis stage, passive pyrolysis stage, and final stage. The water devolatilization was attributed to moisture evaporation and small molecule volatile organic compounds up to 200°C. In line with previous research studies, pine has three main components, hemicellulose, cellulose, and lignin, of which cellulose and hemicellulose account for 65.9–70.9%. Active pyrolysis occurred between 250 and 450 °C with a sharp decrease in weight resulting about 74.09–70.53% of PD and 62.76–56.10% of FPD decomposition of the total weight, respectively. Organic macromolecules such as hemicellulose, cellulose, proteins, and fatty acid decomposition were mainly pyrolyzed in this stage. The third and main stage, i.e., passive stage (450–600°C), is associated with lignin decomposition. The last stage (600–800°C) was attributed with the

Fig. 2 Thermogravimetric characteristics of PD and FPD at different heating rates. **a** Pine sawdust and **b** fermented pine sawdust



degradation of inorganic fragments and secondary coking reactions. At the end process temperature, i.e., 800°C, the residue mass of FPD was 28.90–36.59% in Fig. 2(b) lower than 16.45–20.17% of PD in Fig. 2(a), which indicates the fermentation is conducive to the formation of pine biochar.

As can be seen from Fig. 2, that with the increase in heating rate, the maximum decomposition temperature of the various components shifted to higher temperatures which is due to thermal hysteresis effect. In this section, the PD-X or FPD-X was used to represent samples at dissimilar heating rates (X represents different heating rate). As shown in Table 2, take FPD as example, the T_p was 331.10°C corresponding to 20°C/min. It jumped to 349.61°C for 40°C/min and further shifted to 355.52°C at a 50°C/min heating rate. Besides, the temperature corresponding to the maximum loss of mass varied between 342.96–380.04°C for PD and 331.10–355.52°C. It shifted to lower temperatures and had small temperature fluctuation range after fermentation. The comprehensive pyrolysis index was used to evaluate pyrolysis characteristic. CPI increased with the heating rate from 3.08×10^{-7} at 20°C/min for PD to 9.99×10^{-7} at 50°C/min for PD, indicating that a high heating rate was beneficial for the pyrolysis. Meanwhile, the CPIs of FPD were

6.56×10^{-7} – 16.38×10^{-7} higher than that of PD. A higher CPI value means that the pine sawdust pyrolyzed more vigorously, illustrating fermentation could improve pyrolysis performance and facilitates volatile release (Shahbeig and Nosrati 2020).

Pyrolysis kinetics of PD and FPD by different models

Kinetic study

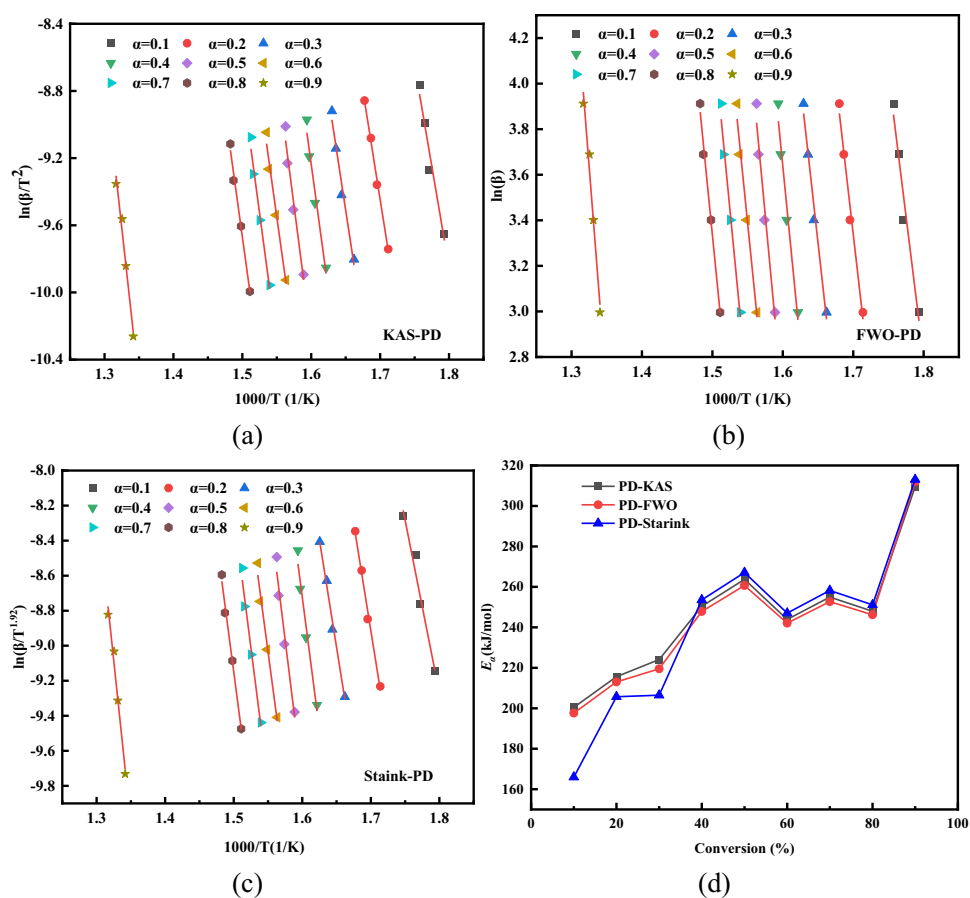
The thermal kinetic parameters of biomass are very important parameters in the efficient design of thermochemical processes as pyrolysis is composed of multistep reaction mechanism along with complex reactions. In this study, pyrolysis kinetics of PD and FPD could be used to further understand pyrolysis behaviors and provide a reference for pyrolysis process and reactors design. Least square method fit plots were formed to assess the relationship between $1/T$ vs $\ln(\beta)$, $1/T$ vs $\ln(\beta/T^2)$, and $1/T$ vs $\ln(\beta/T^{1.92})$ at the conversion rates from 0.1 to 0.9 by a hike of 10% in the FWO, KAS, and Starink models. As shown in Fig. 3 and Fig. 4, the lines were nearly parallel, demonstrating calculation methods were reliable.

Table 2 Pyrolysis characteristics of PD and FPD

Samples	^a T_i (°C)	^b M_f (%)	^c T_p (°C)	^d DTG_{max} (%/°C)	^e DTG_m (%/°C)	^f $T_{1/2}$ (°C)	^g CPI (10^{-7})
PD-20	183.95	17.73	342.96	−0.63	−0.117	64.05	3.08
PD-30	193.84	15.56	362.32	−0.66	−0.121	41.48	4.26
PD-40	202.67	19.32	370.29	−0.73	−0.114	33.51	6.39
PD-50	209.48	18.47	380.04	−0.81	−0.117	21.83	9.99
FPD-20	180.12	35.14	331.10	−0.55	−0.094	45.96	6.56
FPD-30	186.98	28.81	333.96	−0.61	−0.102	44.06	6.51
FPD-40	196.71	35.53	349.61	−0.64	−0.092	25.54	11.91
FPD-50	200.71	34.37	355.52	−0.69	−0.093	18.87	16.38

^a T_i , initial decomposition temperature; ^b M_f , final mass; ^c T_p , peak temperature; ^d DTG_{max} , the maximum mass loss rate; ^e DTG_m , the average mass loss rate; ^f $T_{1/2}$, the interval between two temperatures when $DTG/DTG_{max} = 1/2$; ^gCPI, the comprehensive pyrolysis index, unit is $\%^2 \cdot \text{min}^{-2} \cdot ^\circ\text{C}^{-3}$.

Fig. 3 Plots of the model-free methods of PD **a** KAS, **b** FWO, **c** Starink, and **d**



The three calculation methods followed a similar E_a trend between the conversions of 0.1 and 0.9 with a step-size of 0.1, as shown in Fig. 3(d). The E values were estimated that ranging from 200.44 to 309.53 kJ/mol, 197.63 to 311.97 kJ/mol, and 165.98 to 313.08 kJ/mol with an average of 245.61, 243.51, and 240.91 kJ/mol by KAS, FWO, and Starink models, respectively. E_a values at the beginning are considered low due to the cleavage of contain weak bonds (e.g., O–H) and the elimination of volatile components from PD's surface. After $\alpha = 0.1$, the second pyrolysis stage occurs, accompanied by the generation of various volatiles resulting in different rates of volatile escape. The volatiles evolved to cover the surface of pine sawdust and form carbonaceous char, which acts as a barrier insulating the heat from reaching the surface below resulting in decrease of reaction activity. Ultimately, more energy is required to activate the reaction as conversion increases. When $\alpha = 0.9$, E_a rose sharply. This might be due to deep degradation of lignin and formation of carbon in multi-aromatic ring system.

plot of activation energy vs conversion.

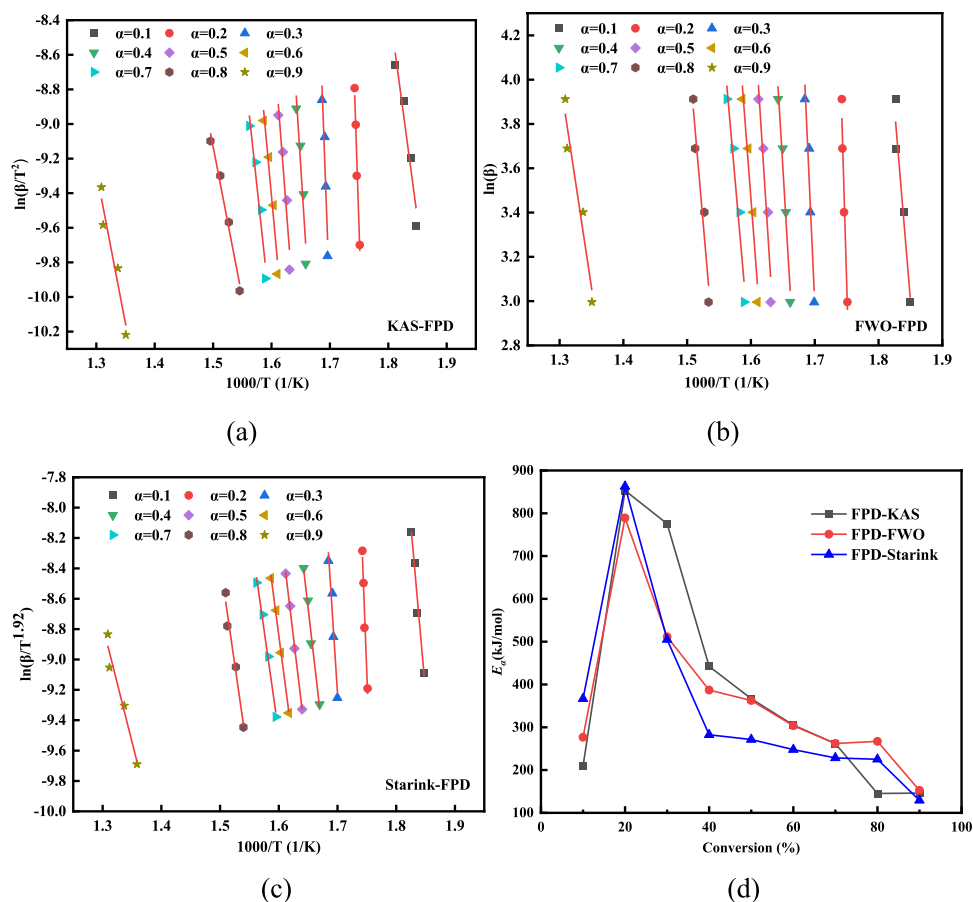
As shown in Fig. 4(d), the activation energies of FPD ranged from 145.34 to 853.13 kJ/mol, 152.59 to 789.19 kJ/mol, and 129.11 to 862.87 kJ/mol attained by KAS, FWO, and Starink method, respectively. E_a values changed

significantly with the increase of α . From $\alpha = 0.1$ –0.3, the activation energies were found to increase significantly. High E_a indicates that some highly endothermic reaction occurred at this conversion point, while a decline of E_a shows the gradual transition of reaction mechanism during the pyrolysis process of fatty acids and proteins. Overall, the average E_a of FPD was higher than that of PD which might be due to the destruction of macromolecule crosslinked structure by fermentation and co-pyrolysis of fermentation product and raw material. In future research, focusing on catalytic or co-pyrolysis may be a suitable way to reduce the pyrolysis activation energy.

Thermodynamic parameters

Table 3 shows the thermodynamic parameters (A , ΔH , ΔG , and ΔS) of PD and FPD at different conversion rates. The pre-exponential factor (A) explains the proper orientation for chemistry reaction to take place. $A < 10^9 \text{ s}^{-1}$ mainly shows the surface reaction, while $A \geq 10^9 \text{ s}^{-1}$ indicates a complex reaction. The enthalpy change (ΔH) reflects the total energy consumed during pyrolysis process for its conversion, while the difference between E_a values and ΔH reflects the reaction's probability. The Gibbs free energy (ΔG) and entropy

Fig. 4 Plots of the model-free methods of FPD. **a** KAS, **b** FWO, **c** Starink, and **d** plot of activation energy vs conversion



(ΔS) exhibit the amount of available energy and the proximity of the reaction system to the equilibrium state.

As shown in Table 3, the A values of PD ranged from 3.77×10^{29} to 2.66×10^{45} by the KAS method, 1.47×10^{29} to 6.01×10^{45} by the FWO method, and 3.54×10^{24} to 8.68×10^{45} by the Starink method. The A values showed that the studied FPD were more complex and had the complicated chemical reaction during pyrolysis due to the complex structure and compositions. Differences of around 5.31 kJ/mol of PD and 5.17 kJ/mol were observed between E_a and ΔH values, showing that product formation would be easier. The average ΔG (83.53–83.61 kJ/mol) of PD was higher when compared to the that of FPD (77.22–77.51 kJ/mol) reflecting the considerable bioenergy potential of samples after fermentation through pyrolysis. Moreover, a wide range of ΔS values indicates complex reaction chemistry.

Biochar of PD and FPD

In the study, all samples of PD and FPD at different temperatures were subjected to adsorption experiments. It was found that PD and FPD samples at 800°C showed better adsorption effect (Table S1). So, PD-800 and FPD-800 were the main object of analysis in Sect. "Biochar of PD and FPD".

FTIR spectra of PD and FPD

The FTIR spectra of two samples are shown in Fig. S1, indicating that biochar consisted of several functional groups. According to prior research, the main functional groups of PD and FPD include hydroxyl, aromatic, aliphatic, and oxygen-containing functional groups. The bands around 3491, 2850, 1750, and 750 cm^{-1} bands are attributed with stretching vibrations of OH, CH_3 , $\text{C}=\text{O}$, and the out-of-plane vibration of C-H, respectively (Jiang et al. 2021). As can be seen, the O–H peaks of PD and FPD were gradually weakened after pyrolysis because of the decomposition of cellulose and lignin. Besides, the content of oxygenated functional group ($\text{C}=\text{O}$) varied greatly. The PD-800 and FPD-800 with abundant groups on the surface exhibit a better MB adsorption capacity.

To eliminate the effect of multi-peak overlap, the FTIR were deconvolved to fit functional group absorption peak information, and then, a qualitative analysis was adopted. The absorption peaks are predominantly hydroxyl in the range of 3700–3000 cm^{-1} , which could be judged to contain alcohols, phenols, and organic acids. The absorption peaks in the range of 3000–2700 cm^{-1} are connected with aliphatic structures (Cai et al. 2019). Several significant spectral

Table 3 Thermodynamic parameters of PD and FPD

Sample	Conversion (α)	KAS			FWO			Starink		
		A	ΔH kJ/mol	ΔS J/mol·K	A	ΔH kJ/mol	ΔS J/mol·K	A	ΔH kJ/mol	ΔS J/mol·K
PD	0.1	3.77E+29	195.76	306.76	1.47E+29	192.94	298.91	3.54E+24	161.30	210.51
	0.2	6.08E+31	210.70	348.42	2.56E+31	208.11	341.21	2.19E+30	200.78	320.78
	0.3	1.04E+33	219.02	371.63	2.25E+32	214.44	358.87	2.85E+30	201.41	322.55
	0.4	6.95E+36	245.20	444.47	2.96E+36	242.65	437.39	2.02E+37	248.39	453.37
	0.5	6.01E+38	258.43	481.26	2.20E+38	255.42	472.91	1.84E+39	261.78	490.58
	0.6	7.97E+35	238.53	425.94	4.28E+35	236.68	420.78	2.28E+36	241.67	434.68
	0.7	3.19E+37	249.49	456.42	1.51E+37	247.24	450.17	9.55E+37	252.76	465.51
	0.8	3.05E+36	242.36	436.59	1.73E+36	240.66	431.86	8.89E+36	245.56	445.49
	0.9	2.66E+45	303.25	605.77	6.01E+45	305.69	612.54	8.68E+45	306.80	615.61
	Average		240.30	83.53		238.20	83.56		235.61	83.61
FPD	0.1	5.83E+32	204.65	368.11	1.49E+43	272.10	567.34	1.12E+57	362.29	832.99
	0.2	3.83E+131	848.38	2259.04	6.29E+121	784.43	2071.72	1.18E+133	858.11	2287.56
	0.3	4.88E+119	770.49	2030.86	1.71E+79	506.37	76.01	1.83E+78	500.05	1237.83
	0.4	4.57E+68	437.34	76.42	1.38E+60	381.84	76.79	1.25E+44	277.53	583.39
	0.5	1.07E+57	361.50	830.69	2.49E+56	357.40	76.98	2.28E+42	266.16	549.86
	0.6	3.59E+47	299.84	77.48	2.03E+47	298.22	77.49	5.68E+38	242.72	480.66
	0.7	8.07E+40	256.60	77.91	8.58E+40	256.77	77.91	5.46E+35	223.09	422.68
	0.8	7.61E+22	139.86	79.59	5.04E+41	261.55	77.85	1.73E+35	219.65	412.53
	0.9	1.01E+23	139.86	79.57	1.02E+24	146.33	79.45	2.26E+20	122.84	125.30
	Average		384.28	77.31		362.78	77.22		341.38	77.51

peaks are fitted at the peaks of 2985–2950, 2840–2720, and 2902 cm^{-1} , and they correspond to the CH_3 asymmetric stretching vibration, CH_2 symmetric stretching vibration, and CH symmetric stretching vibration, respectively (Guo et al. 2021). Most of the absorption peaks in range of 1800–1000 cm^{-1} are oxygen-containing functional groups. The bands at 1630–1540 cm^{-1} and 1010–1280 cm^{-1} are related to the symmetric stretching vibrations of carboxyl groups ($\text{C}=\text{O}$) and the stretching vibrations of alcoholic or carboxylic acid ($\text{C}-\text{O}$) band. The absorption peaks in range of 900–700 cm^{-1} are mainly formed by the benzene ring structure with a single H atom, faintness adjacent H atoms replaced by CH, and the n-alkane side-chain backbone structure (Zhu et al. 2019).

Specific peaks corresponding to the functional group are listed in Table 4. As shown in Fig. 5(a) and Fig. 5(b), the FTIR of PD and FPD are deconvolved into 12 and 11 peaks by Gaussian Fitting with $R_2 > 0.99$, respectively. The OH functional group in PD accounted for 35.78% of the total functional group, mainly hydroxyl-ether oxygen-hydrogen bond and hydroxyl self-associating hydrogen bond, accounting for 25.76% and 10.11%, respectively. After fermentation, the abundance of OH functional groups increased with the emergence of free OH (1.72%) and OH tetramers (16.13%). The proportion of aliphatic functional groups increased significantly from 6.20% of PD to 24.41% of FPD. In addition, the content of methylene increased by 13.02%. The ratio of CH_2 (2935–2919 cm^{-1})/ CH_3 (2975–2950 cm^{-1}) was calculated and found to decrease from 0.48 to 0.45, illustrating that fermentation reduced the length of aliphatic side chains and favored carbon condensation to form aromatic fused rings. The percentage of oxygen-containing functional groups in PD was found more than 50%, but it was decreased by about 15% in biochars after fermentation treatment. The

underlying functional groups of PD changed from $\text{C}=\text{O}$ with 36.66% residence to $\text{C}-\text{O}$ with 16.14% occupancy, and the functional group distributions were also averaged. The content of 1H on the aromatic ring of FPD (1.79%) was higher than that of PD (0.17%). It indicates that fermentation pretreatment is beneficial for side-chain substitution and reduces the number of branch chains.

Ultimately, fermentation pretreatment can improve the distribution of functional groups on the surface of biochar, change the seam abundance of functional groups, reduce the length and number of branched chains, and also promote the formation of aromatic rings in the charring reaction.

Adsorption application study of PD and FPD

The pore structure, as shown in Fig. S2, influenced the relationship between the adsorption capacity of MB and the adsorption time for PD and FPD. Pore characteristics of PD-800 and FPD-800 are tabulated in Table S2. The BET surface areas are 32.82 m^2/g (FPD-800) and 19.69 m^2/g (PD-800). Obviously, fermentation treatment could increase the specific surface area of derived biochar. The average pore sizes of FPD-800 and PD-800 are 8.51 and 8.64 nm, respectively. Then, the Fig. 6 shows the curves of nitrogen adsorption-desorption and the pore size distribution calculated by DFT model. The adsorption amount of nitrogen of FPD-800 is larger than that of PD-800 (refer to details from Fig. 6(a)). As can be seen from Fig. 6(b), both pore sizes of PD-800 and FPD-800 are distributed in the range of mesopores, while pore sizes range from 2 to 17 nm. Noticeably, the pore volume of FPD-800 is higher than that of PD-800. All these results indicate that the biochar derived from fermented pine sawdust may have a larger pore volume, which is conducive to the adsorption application.

Table 4 The groups contents of PD and FPD

Types of functional groups		content (PD, %)		content (FPD, %)	
OH group	Free OH	0	35.87	1.72	33.27
	Self-associated OH	10.11		15.41	
	OH-ether O hydrogen bonds	25.76		0.00	
	Tightly bound cyclic OH tetramers	0		16.13	
Aliphatic groups	$\text{R}-\text{CH}_3$	4.14	6.20	9.75	24.41
	R_3-CH methylene	1.64		14.66	
	R_2-CH_2 alkyl	0.41		0.00	
Oxygen-containing	$\text{C}=\text{O}$ conjugated quinone carbonyl	36.66	55.12	5.19	40.54
	$\text{O}-\text{CH}_3$ methoxy	5.22		1.68	
	Phenolic $\text{O}-\text{H}$	8.33		10.60	
	$\text{C}-\text{O}$ of phenols or ethers	4.10		6.93	
	Aromatic ether $\text{C}-\text{O}$	0.80		16.14	
Aromatic hydrogen	Aromatic hydrogen-1H	0.17	2.81	1.79	1.79
	Aromatic hydrogen-3H	2.64		0	

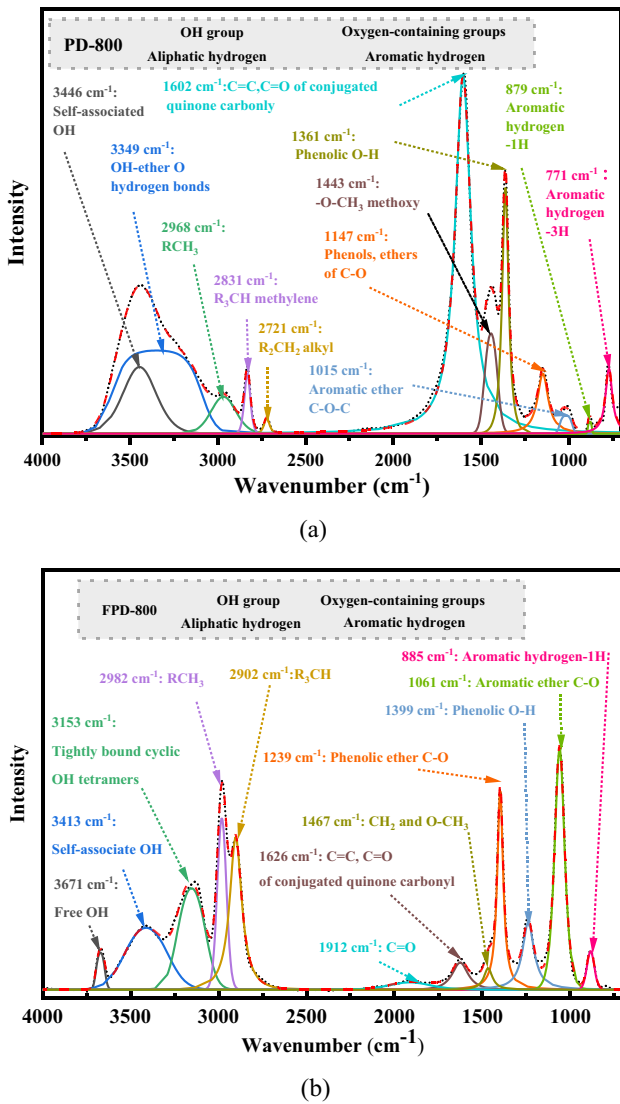
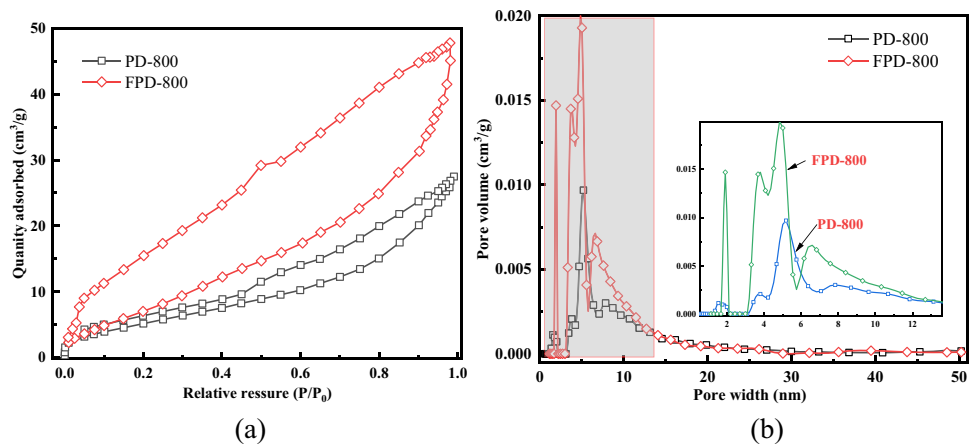


Fig. 5 The curve-fitted IR spectra

Fig. 6 Curves of nitrogen adsorption–desorption (a) and pore size distribution (b)



As shown in Fig. 7, with the increase of adsorption time, the absorbance of MB solution decreased gradually, which indicates that the PD-800 and FPD-800 adsorbed MB. The concentration of MB solution decreased from 5 to 4.24 mg/L (PD-800) and 3.39 mg/L (FPD-800), respectively. Moreover, rapid adsorptions were observed for the first 30 min. The PD-800 obtained adsorption capacity of 0.54 mg/g, while the PDF-800’s adsorption capacity of 1.07 mg/g. The removal of MB was further equilibrated after 180 min obtaining an adsorption capacity of 0.75 mg/g for PD-800. However, the biochars pretreated by fermentation reached stage saturation after 120 min of adsorption, after which the adsorption capacity continued to rise and reached a final saturation after 180 min with a higher adsorption capacity of 0.85 mg/g than that of PD-800.

The multistage adsorption characteristics of the samples illustrated that the adsorption process was conducted in multisteps. In the initial stage, there were plenty of adsorption sites available on PD-800 and FPD-800 surface, MB molecules rapidly diffused to sample surface for surface adsorption and adsorption quantity increased rapidly during the first 30 min. As the time increases, the active sites were gradually occupied and gradually decreased due to the hindered of intermolecular collision and inter-channel extrusion. The adsorption slowly increased after 30 min until reaching the adsorption equilibrium for PD-800. Nevertheless, for FPD-800, under the influence of the concentration of solution and the adsorption force of surface functional groups, MB molecules entered the deep pore network of FPD-800, showing further adsorption. Meanwhile, the MB molecules entered in a stable state of adsorption and desorption.

Adsorption kinetics study of PD and FPD

The adsorption mechanism of samples was determined using pseudo-first-order kinetic, pseudo-second-order kinetic, Elovich, intraparticle diffusion models to fit the

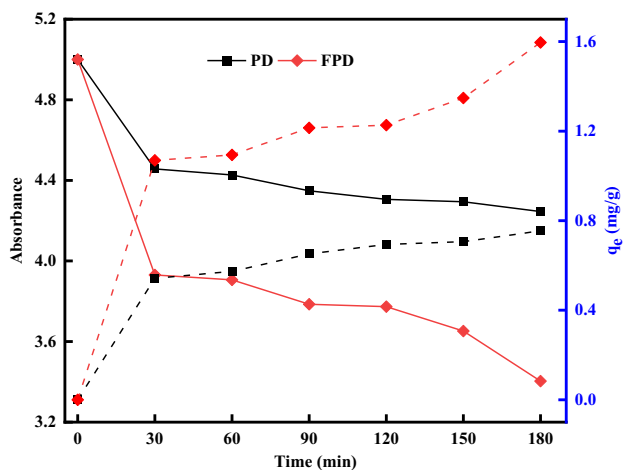


Fig. 7 Effect of reaction time on the adsorption process

experimental data. The fitting results of adsorption kinetics and model parameters are shown in Fig. 8 and Table 5, respectively.

In literature, the adsorption mass transfer kinetics includes external diffusion, internal diffusion, and adsorption in the active adsorbent sites (Chen et al. 2022; Zeng et al. 2022).

In pseudo-first-order kinetic fitting, the R^2 were 0.969 and 0.972 for fitting the adsorption process of PD-800 and FPD-800, reflecting good linear fit. However, deviations could be observed in the experimental equilibrium adsorption capacity and fitted adsorption capacity. The experimental adsorption capacity and calculated adsorption capacity of PD-800 were 0.755 mg/g and 0.347 mg/g, while those of FPD-800 were 1.597 mg/g and 0.669 mg/g, respectively. It could be observed that the pseudo-second-order kinetics model provided a good agreement with the experimental data. The linear fitting effect was excellent showing very slight deviation between the experimental (0.755 mg/g) and the calculated q_e (0.824 mg/g) for PD-800. It can be possibly explained that the MB adsorption process of PD-800 and FPD-800 from surface adsorption to water was mainly controlled by the chemisorption mechanism connected to surface functional groups such as hydroxy groups (π - π) and oxygen-containing functional groups (Lv et al. 2022, Sarkar and Wang 2020). Moreover, as shown in Table 3, the correlation coefficient was 0.986, higher than that of other models, for fitting the adsorption process of FPD-800 using the intra-particle diffusion kinetic equation (Table 3). And, the value of c was greater than 0, indicating that the adsorption includes both diffusion of MB by the aqueous solution towards the external surface of the

Fig. 8 The kinetic models for MB adsorption of a pseudo-first-order, b pseudo-second-order, c Elovich, and d intraparticle diffusion

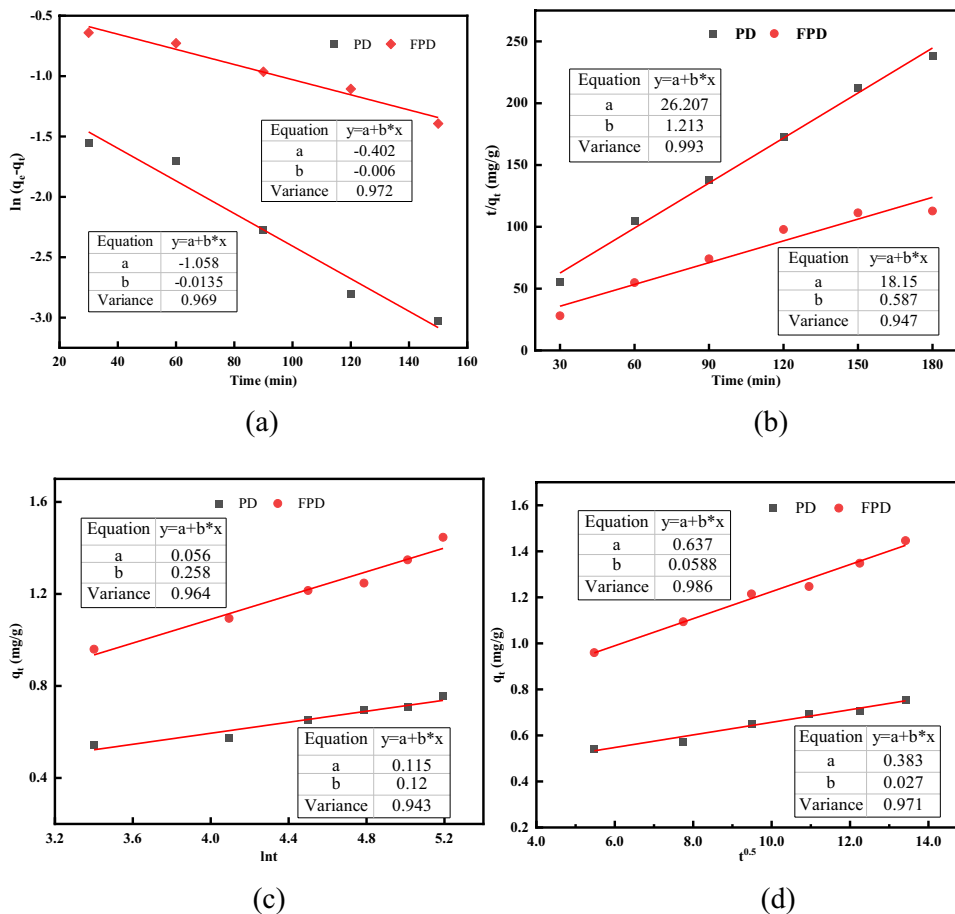


Table 5 Adsorption kinetics parameters of different models

Item	Equation	Parameters	PD-800	FPD-800
		q_e	0.755	1.597
Pseudo-first-order	$\ln(q_e - q_t) = \ln q_e - k_1 t$	$k_1(\text{min}^{-1})$ $q_e(\text{mg/g})$ R^2	0.014 0.347 0.969	0.006 0.669 0.972
Pseudo-second-order	$\frac{t}{q_t} = \frac{1}{k_2 q_e^2} + \frac{t}{q_e}$	$k_2(\text{g}/(\text{mg}\cdot\text{min}))$ $q_e(\text{mg/g})$ R^2	0.056 0.824 0.994	0.019 1.703 0.947
Elovich	$q_t = \frac{\ln(\alpha\beta) + \ln t}{\beta}$	$\alpha(\text{mg}/(\text{g}\cdot\text{min}))$ $\beta(\text{g}/\text{mg})$ R^2	0.313 8.333 0.943	0.321 3.876 0.964
Intraparticle diffusion	$q_t = k_3 t^{0.5} + c$	$k_3(\text{mg}/(\text{g}\cdot\text{min}^{0.5}))$ $c(\text{g}/\text{mg})$ R^2	0.027 0.383 0.971	0.059 0.637 0.986

t , adsorption time (min); q_e , equilibrium adsorption capacity of biochar (mg/g); q_t , adsorption capacity corresponding to time (mg/g); k_1 , rate constant of the pseudo-first-order kinetic equation (min^{-1}); k_2 , rate constant of the pseudo-second-order kinetic equation ($\text{g}/(\text{mg}\cdot\text{min})$); k_3 , diffusion constant ($\text{mg}/(\text{g}\cdot\text{min}^{0.5})$); α , β , the constant of Elovich model; c , thickness constant of the interface layer.

adsorbent and the MB diffusion by the adsorbent pores. Consequently, biochar samples after fermentation pretreatment have larger adsorption capacities, and the adsorption properties shifted from chemisorption to intraparticle diffusion and surface adsorption synergistically.

Fermentation application

Based on above results and discussion, the challenges have been summarized together with future suggestions for the application of fermentation: (a) the characterization study about fermentation feedstocks should have a more detailed classification and strict regulation. (b) It is necessary to establish full evaluation system of fermentation including production of high-value fermentation products, fermentation substrate utilization, and secondary resource recovery of fermentation residues. (c) It is necessary to focus on the multiple co-pyrolysis methods to reduce the pyrolysis energy of fermentation residue, increase the energy substitution of biogas and bio-oil, and directionally regulate the pore structure and functional group distribution of biochar to improve the bioenergy utilization. (d) More research is needed to explore zero-waste fermentation strategy, focusing on energy utilization, environmental benefits, and economic value of fermentation system.

Conclusion

In this study, the physicochemical properties, thermal decomposition kinetics, and biochar properties associated with fermented pine sawdust (FPD) and pine sawdust (PD) were found significantly different. (a) Fermentation pretreatment reduced

the ash content of the sample and increased the content of fixed carbon (from 16.35 to 21.63%) and oxygen content of the raw material (from 49.21 to 62.20%). (b) The CPI and activation energy of FPD were higher than that of PD, elucidating that fermentation could improve pyrolysis performance. (c) Fermentation pretreatment increased the abundance of surface functional groups, reduced the length of aliphatic branch chain (from 0.48 to 0.45), and promoted the formation of aromatic benzene ring carbon, which resulted in increased specific surface area from 19.69 (PD-800) to 32.82 m^2/g (FPD-800). (d) Biochar's characteristics further enhanced its adsorption capacity from 0.755 to 1.597 mg/g (MB as adsorbate), while transforming its adsorption mode into coadsorption of intraparticle diffusion and surface adsorption.

Supplementary Information The online version contains supplementary material available at <https://doi.org/10.1007/s11356-022-25084-0>.

Author contribution Yiteng Zhang, visualization, investigation, writing—original draft; Jun Hu, investigation, methodology data curation; Xingxing Cheng, conceptualization, supervision, project administration; Mudassir Hussain Tahir, writing—review and editing. All authors read and approved the final manuscript.

Funding This work was supported by the Shandong Key Research and Development Plan (NO. 2020CXGC011402), and Shandong Province Natural Science Foundation (NO. ZR2020ME190).

Data availability Data are available from the authors upon request.

Declarations

Ethics approval This is an original article that did not use other information that requires ethical approval.

Consent to participate All authors participated in this article.

Consent for publication All authors have given consent to the publication of this article.

Competing interests The authors declare no competing interests.

References

- Agnihotri N, Gupta GK, Mondal MK (2022): Thermo-kinetic analysis, thermodynamic parameters and comprehensive pyrolysis index of *Melia azedarach* sawdust as a genesis of bioenergy. *Biomass Conversion and Biorefinery*
- Ahmad SFK, Md Ali UF, Isa KM (2019) Compilation of liquefaction and pyrolysis method used for bio-oil production from various biomass: a review. *Environ Eng Res* 25:18–28
- Ahn J, Oh S, Kang YJ, Kim K, Moon S-K, Moon B, Myung S, Kim M-S, Lee YK, Ko K (2021): Effect of oak tree sawdust fermentation period on peanut seed germination, seedling biomass, and morphology. *Horticulturae* 7
- Amenaghawon AN, Anyalewechi CL, Okieimen CO, Kusuma HS (2021) Biomass pyrolysis technologies for value-added products: a state-of-the-art review. *Environ Dev Sustain* 23:14324–14378
- Barzallo-Bravo LA, Carrera-Villacrés D, Vargas-Verdesoto RE, Ponce-Loaiza LK, Correoso M, Gavilanes-Quishpi AP (2019) Biodegradation and post-treatment of effluents by bio-fermentation, an opportunity for energy uses and generation of organic fertilizers from bovine manure. *Intl J Recyc Org Waste Agri* 8:431–438
- Bi H, Wang C, Lin Q, Jiang X, Jiang C, Bao L (2021) Pyrolysis characteristics, artificial neural network modeling and environmental impact of coal gangue and biomass by TG-FTIR. *Sci Total Environ* 751:142293
- Borel LDMS, de Lira TS, Ataíde CH, de Souza Barrozo MA (2020) Thermochemical conversion of coconut waste: material characterization and identification of pyrolysis products. *J Therm Anal Calorim* 143:637–646
- Buessing L, Goldfarb JL (2012) Energy along Interstate I-95: pyrolysis kinetics of Floridian cabbage palm (*Sabal palmetto*). *J Anal Appl Pyrol* 96:78–85
- Cai X, Li J, Liu Y, Hu X, Tan X, Liu S, Wang H, Gu Y, Luo L (2019): Design and preparation of chitosan-crosslinked bismuth ferrite/biochar coupled magnetic material for methylene blue removal. *Int J Environ Res Public Health* 17
- Chen C, Xu Y, Shao J, Zhang Y, Yu M, Sun L, Wang H, Xie Y, Zhu G, Zhang L, Pan L (2022) Waste-converted nitrogen and fluorine co-doped porous carbon nanosheets for high performance supercapacitor with ionic liquid electrolyte. *J Colloid Interface Sci* 616:413–421
- Chhabra V, Bhattacharya S, Shastri Y (2019) Pyrolysis of mixed municipal solid waste: characterisation, interaction effect and kinetic modelling using the thermogravimetric approach. *Waste Manag* 90:152–167
- Feng L, Li Z, Hong C, Xing Y, Qin Y, Lu Y, Zhao X, Lu J (2022): Characteristic analysis of bio-oil from penicillin fermentation residue by catalytic pyrolysis. *Environ Technol*, 1–9
- Fu Y, Que Z, Shi J, Ai X, Zou W (2022) Thermal behavior and gas products of cold rolling oily sludge by TG-MS and Py-EGA/MS. *Energy Rep* 8:763–773
- Gao N, Li A, Quan C, Du L, Duan Y (2013) TG-FTIR and Py-GC/MS analysis on pyrolysis and combustion of pine sawdust. *J Anal Appl Pyrol* 100:26–32
- Guo J, Zheng L, Li Z, Zhou X, Cheng S, Zhang L, Zhang Q (2021): Effects of various pyrolysis conditions and feedstock compositions on the physicochemical characteristics of cow manure-derived biochar. *Journal of Cleaner Production* 311
- Gupta N, Mahur BK, Izrayeel AMD, Ahuja A, Rastogi VK (2022) Biomass conversion of agricultural waste residues for different applications: a comprehensive review. *Environ Sci Pollut Res Int* 29:73622–73647
- He X, Rong P, Liu H, Gan B, Wu D, Li H, Gan R (2022): Co-fermentation of edible mushroom by-products with soybeans enhances nutritional values, isoflavone aglycones, and antioxidant capacity of Douchi Koji. *Foods* 11
- Herath A, Navarathna C, Warren S, Perez F, Pittman CU Jr, Mlsna TE (2022) Iron/titanium oxide-biochar ($\text{Fe}_2\text{TiO}_5/\text{BC}$): A versatile adsorbent/photocatalyst for aqueous Cr(VI), Pb(2+), F(-) and methylene blue. *J Colloid Interface Sci* 614:603–616
- Hoang CN, Yang Z-W, Huang M-Y, Lin K-H, Yang C-M, Nguyen MK (2019) Changes in nutrient and heavy metal content levels of sawdust due to vermicomposting by *Allomyrina dichotoma* subsp. *tunobosonis*. *Biotechnologia* 100:111–114
- Jiang J, Zhang S, Longhurst P, Yang W, Zheng S (2021) Molecular structure characterization of bituminous coal in Northern China via XRD, Raman and FTIR spectroscopy. *Spectrochim Acta A Mol Biomol Spectrosc* 255:119724
- Khiari B, Massoudi M, Jeguirim M (2019) Tunisian tomato waste pyrolysis: thermogravimetry analysis and kinetic study. *Environ Sci Pollut Res Int* 26:35435–35444
- Li Y, Shang H, Cao Y, Yang C, Feng Y, Yu Y (2022): High performance removal of sulfamethoxazole using large specific area of biochar derived from corncob xylose residue. *Biochar* 4
- Liu T, Miao P, Shi Y, Tang KHD, Yap PS (2022) Recent advances, current issues and future prospects of bioenergy production: a review. *Sci Total Environ* 810:152181
- Liu X-J, Li M-F, Singh SK (2021) Manganese-modified lignin biochar as adsorbent for removal of methylene blue. *J Market Res* 12:1434–1445
- Lv D, Wang D, Wang N, Liu H, Zhang S, Zhu Y, Song K, Yang J, Qian Y (2022) Nitrogen and fluorine co-doped TiO_2 /carbon microspheres for advanced anodes in sodium-ion batteries: high volumetric capacity, superior power density and large areal capacity. *J Energy Chem* 68:104–112
- Ma Y, Liu Y (2019) Turning food waste to energy and resources towards a great environmental and economic sustainability: an innovative integrated biological approach. *Biotechnol Adv* 37:107414
- Meng A, Chen S, Long Y, Zhou H, Zhang Y, Li Q (2015) Pyrolysis and gasification of typical components in wastes with macro-TGA. *Waste Manag* 46:247–256
- Nenciu F, Paraschiv M, Kuncser R, Stan C, Cocarta D, Vladut VN (2021): High-grade chemicals and biofuels produced from marginal lands using an integrated approach of alcoholic fermentation and pyrolysis of sweet sorghum biomass residues. *Sustainability* 14
- Ni Z, Bi H, Jiang C, Sun H, Zhou W, Tian J, Lin Q (2022): Investigation of co-combustion of sewage sludge and coffee industry residue by TG-FTIR and machine learning methods. *Fuel* 309
- Sarkar JK, Wang Q (2020): Characterization of pyrolysis products and kinetic analysis of waste jute stick biomass. *Processes* 8
- Shahbeig H, Nosrati M (2020): Pyrolysis of biological wastes for bioenergy production: thermo-kinetic studies with machine-learning method and Py-GC/MS analysis. *Fuel* 269
- Soria-Verdugo A, Morgano MT, Mätzing H, Goos E, Leibold H, Merz D, Riedel U, Stapf D (2020): Comparison of wood pyrolysis kinetic data derived from thermogravimetric experiments by model-fitting and model-free methods. *Energy Conversion and Management* 212
- Tao Q, Li B, Chen Y, Zhao J, Li Q, Chen Y, Peng Q, Yuan S, Li H, Huang R, Wang C (2021) An integrated method to produce fermented liquid feed and biologically modified biochar as cadmium adsorbents using corn stalks. *Waste Manag* 127:112–120

- Tian B, Du S, Guo F, Dong Y, Mao S, Qian L, Liu Q (2021): Synthesis of biomimetic monolithic biochar-based catalysts for catalytic decomposition of biomass pyrolysis tar. *Energy* 222
- Wang Q, Shao J, Shen L, Xiu J, Shan S, Ma K (2022): Pretreatment of straw using filamentous fungi improves the remediation effect of straw biochar on bivalent cadmium contaminated soil. *Environ Sci Pollut Res Int*
- Wang Y, Wang Y, Zhang Z, Turap Y, Wang Y, Wang I, Wang Z, Wang W (2021) Combined hydrothermal treatment, pyrolysis, and anaerobic digestion for removal of antibiotic resistance genes and energy recovery from antibiotic fermentation residues. *Bioresour Technol* 337:125413
- Yao Y, Gao B, Wu F, Zhang C, Yang L (2015) Engineered biochar from biofuel residue: characterization and its silver removal potential. *ACS Appl Mater Interfaces* 7:10634–10640
- Yu Y, Wu J, Ren X, Lau A, Rezaei H, Takada M, Bi X, Sokhansanj S (2022): Steam explosion of lignocellulosic biomass for multiple advanced bioenergy processes: a review. *Renewable and Sustainable Energy Reviews* 154
- Zeng X-Y, Wang Y, Li R-X, Cao H-L, Li Y-F, Lü J (2022): Impacts of temperatures and phosphoric-acid modification to the physico-chemical properties of biochar for excellent sulfadiazine adsorption. *Biochar* 4
- Zhang J, Chen S, Zhang H, Wang X (2017) Removal behaviors and mechanisms of hexavalent chromium from aqueous solution by cephalosporin residue and derived chars. *Bioresour Technol* 238:484–491
- Zhang J, Sekyere DT, Niwamanya N, Huang Y, Barigye A, Tian Y (2022a) Study on the staged and direct fast pyrolysis behavior of waste pine sawdust using high heating rate TG-FTIR and Py-GC/MS. *ACS Omega* 7:4245–4256
- Zhang Y, Cheng X, Wang Z, Tahir MH, Wang Z, Wang X, Wang C (2022b) Full recycling of high-value resources from cabbage waste by multi-stage utilization. *Sci Total Environ* 804:149951
- Zhang Z, Xu G, Wang Q, Cui Z, Wang L (2019) Pyrolysis characteristics, kinetics, and evolved gas determination of chrome-tanned sludge by thermogravimetry-Fourier-transform infrared spectroscopy and pyrolysis gas chromatography-mass spectrometry. *Waste Manag* 93:130–137
- Zhu YM, Gao LJ, Zhao XF, Lü J (2019): Quantitative analysis of refined pitches by curve-fitting of fourier transform infrared spectroscopy spectrum. *spectroscopy and spectral analysis*

Publisher's Note Springer Nature remains neutral with regard to jurisdictional claims in published maps and institutional affiliations.

Springer Nature or its licensor (e.g. a society or other partner) holds exclusive rights to this article under a publishing agreement with the author(s) or other rightsholder(s); author self-archiving of the accepted manuscript version of this article is solely governed by the terms of such publishing agreement and applicable law.